JOURNAL OF SOLID STATE CHEMISTRY **123,** 168–182 (1996)
ARTICLE NO. 0165

Niobium Carbide Synthesis from Niobium Oxide: Study of the Synthesis Conditions, Kinetics, and Solid-State Transformation Mechanism

V. L. S. Teixeira da Silva,*,† M. Schmal,* and S. T. Oyama†,[1]

*NUCAT/PEQ/COPPE/Universidade Federal do Rio de Janeiro, Brazil; †Department of Chemical Engineering, Virginia Polytechnic Institute and State University, Blacksburg, Virginia 24061-0211

Received October 23, 1995; in revised form January 25, 1996; accepted January 29, 1996

The carburization of B-niobium oxide (B-Nb_2O_5) to niobium carbide (NbC) in 20% (v/v) CH_4/H_2 was studied at temperature-programmed conditions. The reaction required high temperatures, greater than 1370 K, and variations of heating rate (0.04–0.17 K s^{-1}) and molar space velocity (400–1600 h^{-1}) had only a minor effect on the product specific surface area (S_g). In the course of the transformation S_g increased from 1 m^2g^{-1} to about 20 m^2g^{-1}, and scanning electron microscopy showed the development of macropores of about 100 nm. The progress of the reaction was followed by mass spectroscopic analysis of the gaseous products, which identified two distinct stages. X-ray diffraction analysis of reaction intermediates showed that in the first stage B-Nb_2O_5 was reduced to NbO_2, and in the second stage NbO_2 was simultaneously reduced and carburized to NbC. The first reduction occurred by a nucleation mechanism with an activation energy of 100 kJ mol^{-1}. Independent experiments with NbO indicated that it was not involved in the reaction pathway. However, X-ray photoelectron spectroscopy revealed the presence of an oxycarbide phase which was probably the intermediate in the final transformation. Overall the reaction took place by the following steps:

$$\text{B-Nb}_2\text{O}_5 \xrightarrow[\text{fast}]{} \text{NbO}_2 \xrightarrow[\text{slow}]{} [\text{NbO}_x\text{C}_y] \xrightarrow[\text{fast}]{} \text{NbC}.$$

The oxycarbide phase transformed rapidly to the product NbC and was not observable as a bulk phase by XRD. © 1996 Academic Press, Inc.

INTRODUCTION

Transition metal carbides and nitrides have widespread applications because of their unique physical properties, such as high melting points, hardness, electrical conductivity, and superconductivity (1). In catalysis, the materials have attracted attention because they display activities similar to those of the noble metals of Group 8–10 for a variety of reactions such as ammonia synthesis (2), hydrogenation (3–5), methanation (6, 7), isomerization (8–11), and hydrotreating (12–21).

The application of transition metal carbides and nitrides as practical catalysts requires their preparation with high specific surface areas (S_g). This has been achieved by the development of a temperature-programmed method of synthesis (22) which produces materials with S_g of 50–200 m^2/g (23–27).

Most of the work dealing with the application of transition metal carbides and nitrides to catalysis has focused on Mo_2C (28–30), Mo_2N (14, 24, 29), and WC (14, 24). In contrast to the substantial accumulation of data in these systems, very limited information is available on the NbC system. A previous study with a low S_g material indicated poor activity of NbC in quinoline hydrodenitrogenation, but the material was likely to have been contaminated by surface carbon (27).

Five solid single-phase regions exist in the niobium–carbon system: a solid solution of carbon in niobium (bcc), Nb_2C (hcp), NbC (fcc), ζ-Nb_4C_{3-x}, and ζ-NbC_{1-x} (31–33). The compositional range of Nb_2C is very limited at low temperatures, whereas NbC varies from $NbC_{0.70}$ to $NbC_{0.99}$ (31). The ζ-phases have a close packed metal atom stacking sequence of 12 layers per unit cell (ABABCACABCBC...) (33). Industrial production of NbC makes use of Nb_2O_5/C mixtures and heating temperatures of 2073–2273 K leading, consequently, to the formation of materials of low S_g.

In the present paper we report the production of low surface area NbC (S_g = 14–21 m^2g^{-1}) using the temperature-programmed reaction (TPR) between a niobium oxide precursor and a carburizing mixture consisting of 20% (v/v) CH_4/H_2. The solid state transformation of Nb_2O_5 to NbC was investigated with mass spectroscopy to follow the progress of the reaction. X-ray diffraction (XRD), tem-

[1] To whom correspondence should be addressed.

0022-4596/96 $18.00

perature-programmed oxidation (TPO), scanning electron microscopy (SEM), X-ray photoelectron spectroscopy (XPS), and adsorption techniques were used to characterize the intermediates and products.

EXPERIMENTAL

The gases employed in this study were He, O_2, N_2, CO, CO_2, 0.5% (v/v) O_2/He, and 20% (v/v) CH_4/H_2 (all from Linde, UHP grade). He, H_2, N_2, CO, CO_2, and 20% (v/v) CH_4/H_2 were passed through water/oxygen-removing purifiers positioned in the line between the gas cylinders and the reactor.

The chemicals used were all from Johnson Matthey Electronics. Nb_2O_5 (99.9%, B-phase), NbO_2 (99.0%), NbO (99.0%), and NbC (99.0%) were used as received.

Temperature-programmed reaction, temperature-programmed oxidation, and adsorption experiments were carried out in a U-shaped quartz reactor of 15 mm o.d. placed in a furnace (Hoskins, 550W) controlled by a temperature programmer (Omega Model CN2000). A local chromel-alumel thermocouple monitored the temperature of the sample which was recorded by a computer (Thoroughbred, 80386SX-16) through a RS-232 board. Simultaneously, data from a mass spectrometer (Ametek/Dycor Model MA100) was registered into the computer through an A/D board. Lag time due to flow between reactor and mass spectrometer was on the order of seconds, which was negligible in the time scale of the experiments.

In a typical TPR experiment, 400 mg (1505 μmol) of Nb_2O_5 with $S_g = 1\ m^2\ g^{-1}$ were contacted with the reactant 20% (v/v) CH_4/H_2 flow, while the temperature was raised linearly from room temperature (RT) to a final temperature (T_f) using a desired heating rate ($\beta = 0.0417$, 0.0833, 0.125, and 0.1667 K s^{-1}). For each one of these β, three values of flow of the 20% (v/v) CH_4/H_2 mixture were used, 250 $cm^3\ min^{-1}$ (167 μmol s^{-1}), 500 $cm^3\ min^{-1}$ (333 μmol s^{-1}), and 1000 $cm^3\ min^{-1}$ (667 μmol s^{-1}), yielding molar space velocities of 400 h^{-1}, 800 h^{-1}, and 1600 h^{-1}, respectively.

During the TPR synthesis, the effluent gases from the reactor were sampled into the mass spectrometer chamber through a variable leak valve (Granville Phillips Model 203) and the masses 2 (H_2), 15 (CH_4), 18 (H_2O), 28 (CO), and 44 (CO_2) were monitored. To determine the synthesis condition to be used, an experiment was done raising the temperature uniformly from 298 to 1373 K using a heating rate of 0.1667 K s^{-1}. The mass spectrometer indicated that even at the final temperature of 1373 K carbon monoxide formation was continuing, and for this reason the temperature was kept at 1373 K for 0.7 h until the CO signal returned to baseline. All of the syntheses presented in this work followed a similar procedure.

Once the carburization process was over, the gas flowing through the reactor was changed from the 20% (v/v) CH_4/H_2 mixture to a flow of pure He (200 $cm^3\ min^{-1} \approx 133\ \mu$mol s^{-1}) and the reactor was quenched by quickly removing the furnace. After the reactor was cooled to RT, the surface was characterized by the irreversible chemisorption of CO at RT and physisorption of N_2 at liquid nitrogen (LN) temperature. Irreversible CO chemisorption is a technique used in catalysis to titrate surface metal atoms. The measurement was done by injecting pulses of CO through a sampling valve using He as a carrier and the total CO uptake was calculated by referring the areas under the CO signal peaks to the known quantity of 38 μmol for a single peak.

Surface area measurements were done immediately after the CO chemisorption by a similar flow technique using a 30% (v/v) N_2/He mixture. This gas mixture was passed over the sample maintained at LN temperature and the amount of physisorbed N_2 was obtained by comparing the area of the desorption peak with the area of calibrated N_2 pulses containing 38 μmol N_2/pulse. The S_g was then calculated from the single-point BET equation (34).

After CO chemisorption and BET measurements, the gas flowing through the reactor was switched to a 0.5% (v/v) O_2/He mixture to passivate the carbide. The passivation procedure deposited a layer of oxygen on the surface to allow the product to be taken out of the reactor without undergoing bulk oxidation.

Temperature-programmed oxidation experiments were done mainly to determine the total amount of carbon present in the synthesized NbC samples. This technique was similar to TPR but, instead of the methane/hydrogen mixture, utilized a 10% (v/v) O_2/He mixture at a flow rate of 55 $cm^3\ min^{-1}$ (33 μmol s^{-1}). The oxidizing gas mixture was passed over NbC, usually 100 mg (955 μmol), while the temperature was raised linearly at a rate of 0.1667 K s^{-1} from RT to 1123 K. During the heating process, the effluent gases from the reactor were leaked into the mass spectrometer chamber and masses 4 (He), 18 (H_2O), 28 (CO), 32 (O_2), and 44 (CO_2) were monitored continuously following the progress of the oxidation. Once the final temperature of 1123 K was reached, the reactor was cooled to RT under the same mixture by quickly removing the furnace. Calibration pulses of CO and CO_2 of a known quantity (38 μmol) were then injected through a sampling valve using the 10% (v/v) O_2/He as a carrier. The total formation of CO and CO_2 during the TPO analysis was then calculated by referring the areas under the CO and CO_2 peaks to the areas of the pulses of known quantity. In cases where CO and CO_2 were produced simultaneously the raw CO signal was corrected for the fragmentation of CO_2 by a point by point method. With these corrections the TPO technique could be used quantitatively.

Powder X-ray diffraction (XRD) of the passivated samples was carried out using a diffractometer (Siemens,

TABLE 1
Summary of Preparation Conditions and Sample Identification (T_{final} = 1373 K)

Molar space velocity (h^{-1})	Heating rate (Ks^{-1})	Code of the sample
400	0.0417	**400-2.5**
	0.0833	**400-5.0**
	0.1250	**400-7.5**
	0.1667	**400-10**
800	0.0417	**800-2.5**
	0.0833	**800-5.0**
	0.1250	**800-7.5**
	0.1667	**800-10**
1600	0.0417	**1600-2.5**
	0.0833	**1600-5.0**
	0.1250	**1600-7.5**
	0.1667	**1600-10**

Model D500 with a CuKα monochromatized radiation source) operated at 40 kV and 30 mA. X-ray photoelectron spectroscopy (XPS) spectra of the passivated samples were taken with a Perkin–Elmer PHI 5300 spectrometer using a magnesium $K\alpha$ X-ray source (1253 eV) operated at 15 kV with an emission current of 20 mA and a take-off angle of 45°. Typical operating pressures were below 1.33×10^{-5} Pa. Wide scan XPS spectra were obtained on each sample analyzed using the carbon 1*s* photopeak at 284.6 eV for calibration. The purpose of the wide scan was to insure that all major species present in the top 5 nm of the sample were detected. Narrow scan XPS spectra were subsequently obtained on any element to obtain precise values of binding energies. Finally, scanning electron microscopy (JEOL Model 1200X) was used to investigate the external morphology of the intermediates formed during the carburization process.

RESULTS

Table 1 lists and codifies the experimental conditions of the compounds synthesized by TPR. A code with a general form XXX-HR is used with the first field, XXX, representing the molar space velocity used, and the second, HR, representing the heating rate β employed during the TPR synthesis.

Figure 1 shows the water (m = 18) and carbon monoxide (m = 28) formation profiles resulting from the carburization of Nb_2O_5 using a molar space velocity of 400 h^{-1}. The water formation profile consists of a small shoulder at around 900–1050 K, a major peak which is over before T_f, and a second water peak which, depending on the heating rate employed, has its maximum either in the isothermal region at 1373 K or in the temperature-programmed region. As expected from TPR theory (35, 36), the maxima of the water formation peaks (T_{max}) shift to lower temperatures as β is decreased from 0.1667 K s^{-1} to 0.0417 K s^{-1}. On the other hand, the carbon monoxide signal consists of a broad peak which occurs almost entirely in the isothermal region at 1373 K, but with a maximum appearing earlier with decreasing heating rate.

Figure 2 shows the XRD patterns of the compounds synthesized with a molar space velocity of 400 h^{-1} and compares them with those of a commercial carbide and the starting niobium oxide. It is clear from this figure that no reflections from the oxide are present in the synthesized materials and comparison with standard spectra from a powder diffraction file (37) confirms that these compounds are NbC with a rocksalt structure. The main difference between the patterns of the synthesized carbides and that of the commercial carbide is a change in intensity between the (111) and (200) planes, the latter being more intense in the commercial carbide while the former is slightly more intense in the synthesized materials. This difference can be attributed to a small preferential formation of the (111) planes during the synthesis of the samples.

Doubling the molar space velocity from 400 to 800 h^{-1} does not result in new details in either the water or the carbon monoxide formation profiles as can be seen in Fig.

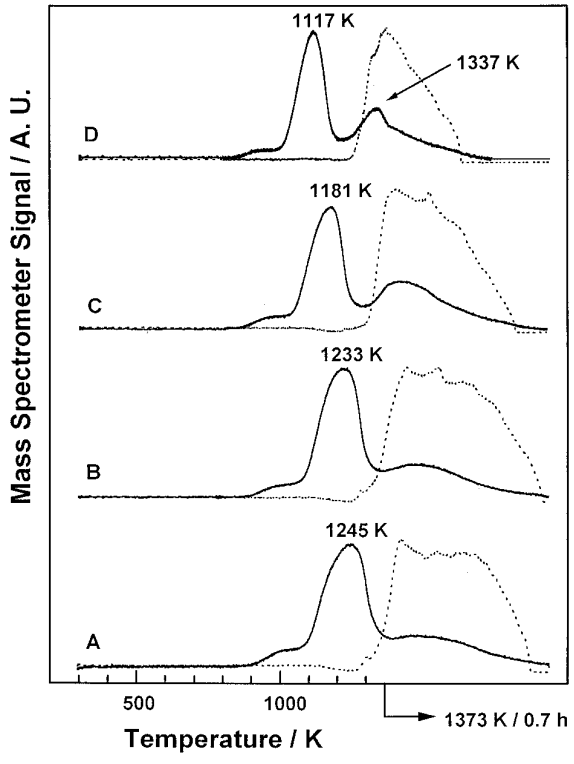

FIG. 1. Water (solid line) and carbon monoxide (dotted line) formation profiles during TPR using a molar space velocity of 400 h^{-1}. (A) 0.1667 K s^{-1}; (B) 0.125 K s^{-1}; (C) 0.0833 K s^{-1}; (D) 0.0417 K s^{-1}.

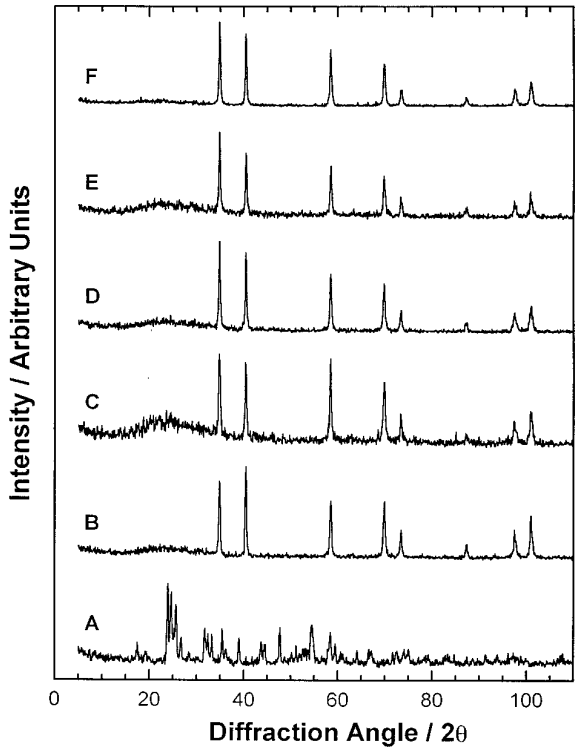

FIG. 2. X-ray diffraction patterns of the carbides synthesized by TPR using a molar space velocity of 400 h^{-1}: (C) 0.1667 K s^{-1}; (D) 0.125 K s^{-1}; (E) 0.0833 K s^{-1}; (F) 0.0417 K s^{-1}. Comparison with (A) B-Nb_2O_5 and (B) commercial NbC.

3. However, comparison of the water profiles presented in Figs. 1 and 3 shows that the synthesis conducted with a molar space velocity of 800 h^{-1} (Fig. 3) has lower T_{max} than the synthesis carried out with 400 h^{-1} (Fig. 1) for the same β. Moreover, Fig. 3 shows that for β of 0.0833 and 0.0417 K s^{-1}, the second water formation peak has its maximum in the temperature-programmed region.

The positive effect of doubling the molar space velocity from 400 to 800 h^{-1} can also be seen in the carbon monoxide profiles presented in Fig. 3. The obtained profile for β of 0.1667 K s^{-1} using a molar space velocity of 800 h^{-1} (Fig. 3A) is somewhat similar in shape to that obtained using a space velocity of 400 h^{-1} and β of 0.0417 K s^{-1} (Fig. 1D). However, as β is decreased from 0.1667 to 0.0417 K s^{-1}, there is a big shift in the position of the maximum of the carbon monoxide peak from the isothermal region at 1373 K to the temperature-programmed region, and also a change in shape. If the water and carbon monoxide profiles presented in Fig. 3D are compared, it can be seen that the carbon monoxide peak is associated with the second water formation peak, indicating that both reduction (water formation) and carburization (carbon monoxide formation) are occurring simultaneously. The absence of any carbon monoxide formation during the first water formation peak indicates that this stage of the transformation consists in a simple reduction of the B-Nb_2O_5 precursor. The XRD patterns of the compounds synthesized with a molar space velocity of 800 h^{-1} were similar to those shown in Fig. 2, and for this reason are not presented.

Figure 4 presents the water formation profiles obtained when the molar space velocity of synthesis has been further increased to 1600 h^{-1}. In agreement with the earlier trends, the increase in space velocity resulted in lowering T_{max} for both the first and second water formation peaks. Regarding the carbon monoxide formation profiles, it can be seen in Fig. 4 that when β of 0.1667 and 0.125 K s^{-1} are used, 90% of the carbon monoxide formation occurs in the isothermal region at 1373 K. Decreasing the heating rate from 0.125 K s^{-1} to 0.0833 and 0.0417 K s^{-1} causes not only a significant shift in the maximum of CO formation from the isothermal region to the temperature-programmed region, but also a splitting in the peak with formation of two well-defined maxima at 1241 and 1285 K as shown in Fig. 4D. XRD patterns of the compounds synthesized using a molar space velocity of 1600 h^{-1} were similar to those of Fig. 2 and again are not presented.

A typical temperature-programmed oxidation (TPO) plot is presented in Fig. 5 and shows the traces for the formation of CO and CO_2, and consumption of O_2. While

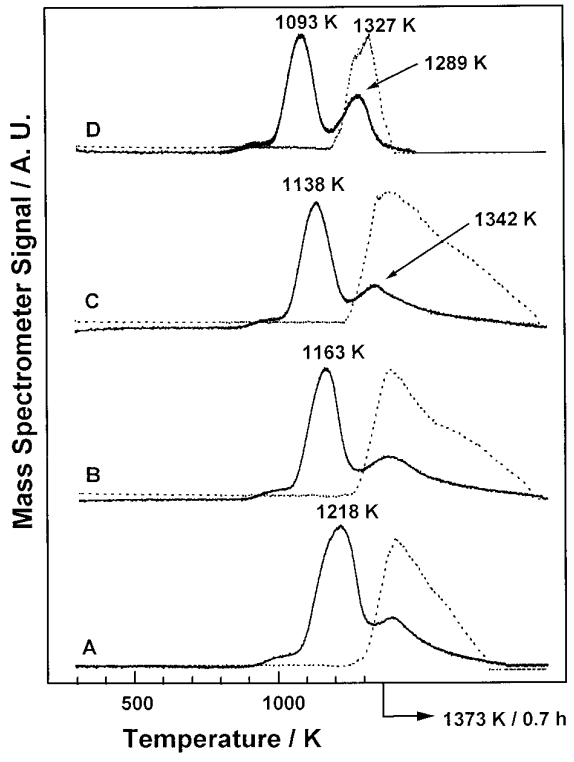

FIG. 3. Water (solid line) and carbon monoxide (dotted line) formation profiles during TPR using a molar space velocity of 800 h^{-1}. (A) 0.1667 K s^{-1}; (B) 0.125 K s^{-1}; (C) 0.0833 K s^{-1}; (D) 0.0417 K s^{-1}.

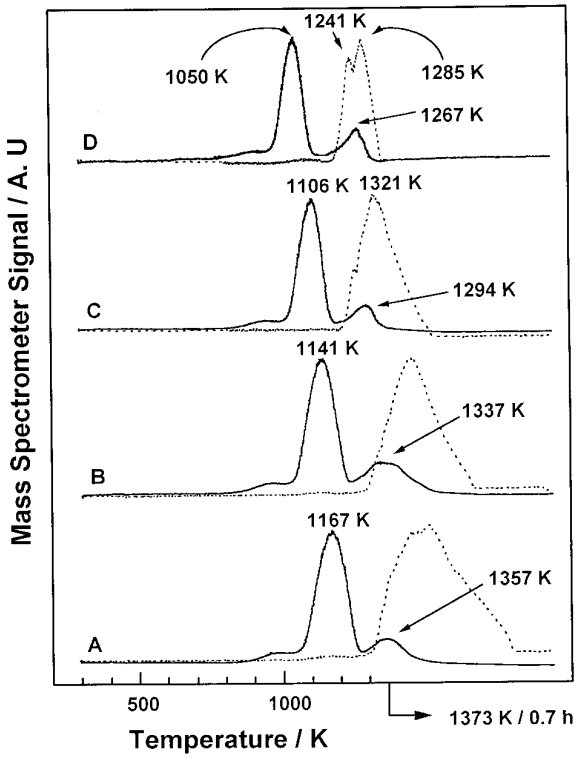

FIG. 4. Water (solid line) and carbon monoxide (dotted line) formation profiles during TPR using a molar space velocity of 1600 h^{-1}. (A) 0.1667 K s^{-1}; (B) 0.125 K s^{-1}; (C) 0.0833 K s^{-1}; (D) 0.0417 K s^{-1}.

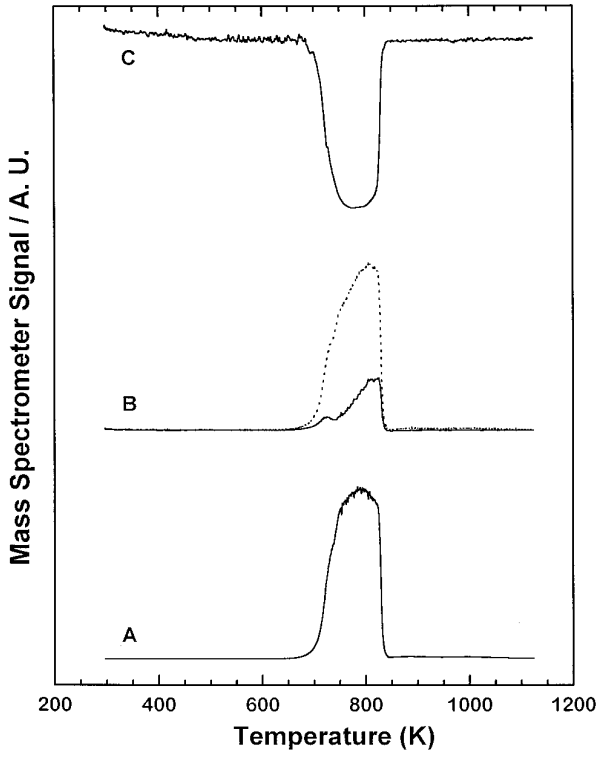

FIG. 5. Carbon dioxide formation (A), carbon monoxide formation (B) (dotted line is the raw signal and the solid line is the corrected one), and oxygen consumption (C) during TPO using a 10%(v/v) O_2/He mixture.

the CO_2 and O_2 profiles consist of single peaks with maxima of formation and consumption at 800 K, the signal of the raw CO formation is somewhat different, presenting a shoulder at 750 K. When the raw CO signal is corrected taking into account the fragmentation of CO_2, the single peak profile becomes a less intense, two-peak profile with maxima at 722 and 809 K, the weak signal indicating little CO formation during the oxidation. All of the carbides listed in Table 1 presented similar TPO profiles to those shown in Fig. 5, with little changes either in the temperature of the maxima of the CO, CO_2, and O_2 or in the shape of the profiles.

XRD analysis of the solids after TPO analysis revealed only the presence of B-Nb_2O_5 indicating total oxidation of the carbide. Since the oxidation NbC $\rightarrow$ B-Nb_2O_5 is complete, the amount of CO and CO_2 formed during TPO allows measurement of total carbon content.

Table 2 reports S_g, irreversible CO uptake, carbon weight obtained by TPO, and crystallite and particle sizes. Crystallite sizes were obtained using the Scherrer equation, $D_C = K\lambda/B\cos(\theta)$, where λ is the wavelength of the X-ray radiation, 0.154 nm, B is the width of the peak at half maximum corresponding to the (111) plane and corrected for instrumental broadening (0.1°), θ is the Bragg angle, and K is a constant taken to be 0.9. Corresponding particles sizes were calculated from the equation $D_P = 6/(S_g\,\rho)$, where ρ is the density of the solid (ρ = 7.82 g/cm^3) and S_g is the specific surface area. Table 2 shows that all of the synthesized carbides have low S_g (14–21 m^2g^{-1}) and low CO uptakes. Since the theoretical weight composition for NbC is 88.56 wt% of Nb and 11.4 wt% of C, the table

TABLE 2
Surface Properties of the Carbides Synthesized by TPR

Carbide	Surface area (m^2 g^{-1})	CO uptake (μmol g^{-1})	C amount (wt%)	D_C (nm)	D_P (nm)
400-2.5	17	6	18.62	24	47
400-5.0	14	4	18.15	23	57
400-7.5	18	6	18.47	33	42
400-10	18	5	18.69	25	43
800-2.5	18	8	18.58	34	43
800-5.0	17	9	18.44	24	47
800-7.5	21	7	18.27	23	37
800-10	17	8	18.45	25	47
1600-2.5	20	10	18.70	30	39
1600-5.0	21	10	18.63	30	37
1600-7.5	20	12	18.52	32	37
1600-10	20	10	18.58	30	37

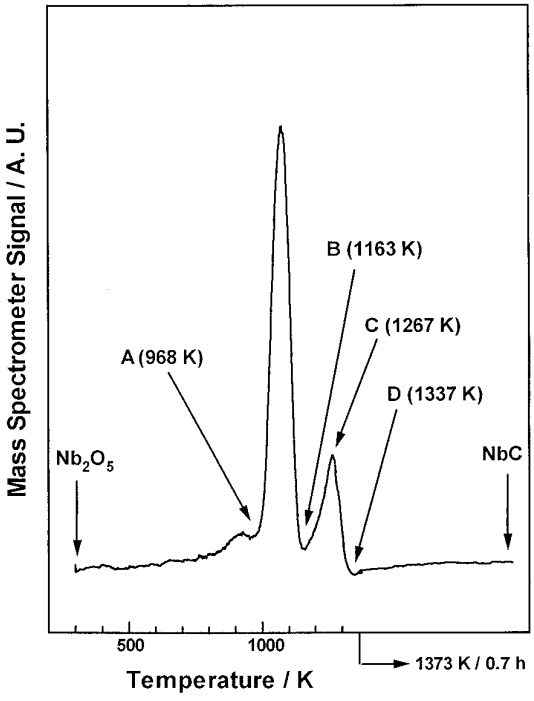

FIG. 6. Points in the water formation profile where the carburization reaction was stopped in order to investigate the intermediates in the solid-state transformation $Nb_2O_5 \rightarrow NbC$.

also shows that all of the synthesized carbides contain excess carbon.

Analysis of the water formation profile in the synthesis of the sample **1600-2.5** (Fig. 6) shows three distinct regions: the first starting at RT and going to 968 K (point A) is characterized by a small shoulder; the second between 968 and 1163 K (points A and B) contains the first water formation peak; and finally, the third region occurring between 1163 and 1337 K (points B and D) contains the second water formation peak. It should be noted that point C for the water formation peak in Fig. 6 corresponds to the start of the carbon monoxide peak profile.

In order to investigate the intermediate stages of transformation, separate experiments were done using the same conditions as **1600-2.5** but stopping the reaction at points A–D (Fig. 6). Interruption of the reaction was done by switching the 20% (v/v) CH_4/H_2 mixture to pure He and quenching the reactor quickly by removal of the furnace. Once RT was reached, CO chemisorption and S_g measurements of the intermediates were taken (Table 3). The samples were subsequently passivated and submitted to XRD, XPS, and SEM analysis.

Figure 7 presents the XRD analysis of the products obtained after stopping the reaction at different stages (points A–D Fig. 6) and shows that the transformation of the Nb_2O_5 starting material to the carbide occurred by formation of NbO_2. The XRD patterns of standards are reported at the bottom for comparison.

The SEM pictures (Fig. 8) of the intermediates A–D as well as the Nb_2O_5 starting material and NbC final product (**1600-2.5**) show that during the transformation $Nb_2O_5 \rightarrow$ NbC the size of the particles does not change substantially; all the compounds are composed of big crystallites. Moreover, Fig. 8 also shows that the external form of the starting material is preserved during the solid-state transformation. However, if the SEM pictures of the starting Nb_2O_5 and NbC final product are compared, a big difference in morphology is seen: while the Nb_2O_5 starting material is constituted of solid, nonporous crystallites, the NbC final product crystallites present voids which probably are responsible for the increase in surface area from 1 to 20 $m^2\ g^{-1}$.

The intermediates A through D, the Nb_2O_5 starting material, and the NbC product were examined by XPS. Figure 9 shows their niobium, carbon, and oxygen narrow-scan spectra. The Nb 3*d* photoemission of the starting material and intermediate A are composed of a doublet at binding energies of 207.1 eV ($Nb_{3d5/2}$) and 209.8 eV ($Nb_{3d3/2}$), characteristic of Nb_2O_5 (38–40). The Nb 3*d* XPS spectrum of intermediate B consists of two doublets (not deconvoluted in the figure), the first with binding energies of 206.0 eV ($Nb_{3d5/2}$) and 209.0 eV ($Nb_{3d3/2}$) corresponding to NbO_2 (40), and the second with binding energies of 202.5 eV ($Nb_{3d5/2}$) and 205.2 eV ($Nb_{3d3/2}$) characteristic of NbC (41). Intermediate C shows similar features with a first doublet at 205.9 and 208.8 eV (NbO_2),and a second doublet at 202.5 and 205.2 eV (NbC). Intermediate D shows further evolution of the spectra with the first doublet at 205.4 eV ($Nb_{3d5/2}$) and 208.5 eV ($Nb_{3d3/2}$) and the second doublet at 202.5 and 205.2 eV (NbC). The first doublet has values intermediate between NbO_2 and NbO (40). Finally, the Nb 3*d* spectrum of the product presents only peaks characteristic of NbC (41).

Figure 9 shows for all compounds a strong C 1*s* feature with binding energy of 284.6 eV. This photopeak is due to surface carbon contamination of the materials due to their

TABLE 3
Surface Properties of the Intermediates during the $Nb_2O_5 \rightarrow$ NbC Reaction

Sample[a]	T (K)[b]	S_g ($m^2\ g^{-1}$)	CO uptake (μmol g^{-1})
Nb_2O_5	300	1	0
A	968	1	0
B	1163	2	0
C	1237	11	5
D	1337	15	7
NbC (**1600-2.5**)	1373	20	10

[a] In accord with Fig. 6.
[b] Final reaction temperature.

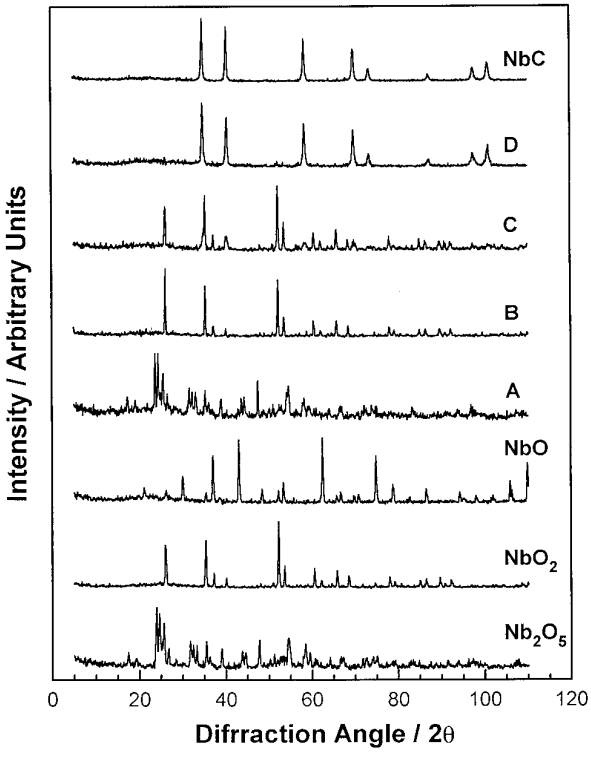

FIG. 7. X-ray diffraction patterns of the products obtained by interruption of the commercial B-Nb_2O_5 carburization reaction. The patterns of NbO_2 and NbO were interspaced for comparison.

exposure to the atmosphere. On the other hand, the C 1*s* spectra of the intermediates A, B, C, and D and the NbC product present a second peak in the binding energy region 283.2–282.1 eV. The intensity of this new photopeak increases as the reaction proceeds toward carbide formation.

Finally, Fig. 9 shows that all of the compounds have O 1*s* peaks with binding energy of 530.0 eV, and that the intensity of these features decreases with increasing extent of carbide formation.

Because NbO_2 was identified as an intermediate in the transformation of Nb_2O_5 to NbC, two additional experiments were carried out with NbO and NbO_2 as starting materials to further investigate their role in the synthesis of NbC. The same conditions as before (**1600-2.5**) were used.

Figure 10A shows the CO formation signal obtained during TPR when NbO was used as a precursor in the synthesis. During this experiment there is no formation of water.

The CO signal is completely different from that of **1600-2.5** (Fig. 4D) obtained under the same experimental conditions, and presents not only a much lower temperature for the maximum of CO formation but also a completely different profile. It consists of a peak with T_{max} at 1182 K and a broader peak which starts near the end of the temperature-programmed region and extends out into the isothermal region and does not return to the baseline even after 0.7 h at the final temperature of 1373 K. The obtained product had a S_g of 3 $m^2\ g^{-1}$ and a null CO chemisorption. In contrast, the CO signal obtained during the synthesis of **1600-2.5** is composed of two peaks which lie completely in the temperature-programmed region.

Figure 10B presents the XRD patterns of NbO (I), commercial NbC (II), and the compound synthesized by TPR using NbO as a precursor (III). It is clear from the figure that the compound obtained from NbO is not a pure carbide since its diffraction pattern retains several of the characteristic reflections of NbO (marked with *).

When NbO_2 was used as a precursor in the TPR synthesis of NbC, a CO formation profile similar to that obtained during the synthesis of the carbide **1600-2.5** was obtained. Figure 11A shows the CO formation profile for the synthesis using NbO_2 as starting material and experimental conditions of SV_{molar} = 1600 h^{-1} and heating rate of 0.0417 K s^{-1}. During this synthesis, a very weak signal due to water formation was observed in the same range of temperature as CO evolution, indicating the simultaneous occurrence of reduction and carburization processes.

Comparing the CO formation profiles presented in Figs. 4D and 11A it can be seen that both consist of two peaks, both lie in the temperature-programmed region, and both show a complete return of the signal to the baseline before T_f. However, there are differences. The peaks for the NbO_2 starting material occur at slightly lower temperatures and present an inversion in the intensity of the two peaks, the first being more intense than the second.

The diffraction patterns of NbO_2, commercial NbC, and the compound synthesized by carburization of NbO_2 are presented in Fig. 11B (I), (II), and (III), respectively. Comparison of the patterns (II) and (III) reveals that the obtained compound is a pure carbide. The obtained carbide had S_g = 5 $m^2\ g^{-1}$ and CO_{uptake} = 0 μmol g^{-1}.

DISCUSSION

Influence of the Variation of the Heating Rate and Space Velocity over S_g

Several studies of Mo_2N (15, 16, 18, 24, 27) and Mo_2C (26, 27) synthesis using the TPR method show that the use of low heating rates and high space velocities lead to materials of high specific area (S_g). While it is well accepted that the use of low heating rates allows the reaction to take place at low temperatures in agreement with the TPR theory, the positive effect of space velocity is still a subject of controversy: some authors propose that the use of high space velocities removes by-product water from the vicinity of the reacting solid avoiding hydrothermal sintering (16, 42, 43), and others suggest that product inhibition of reduction is avoided with a low concentration of water (44).

However, in contrast to the syntheses of Mo_2C and

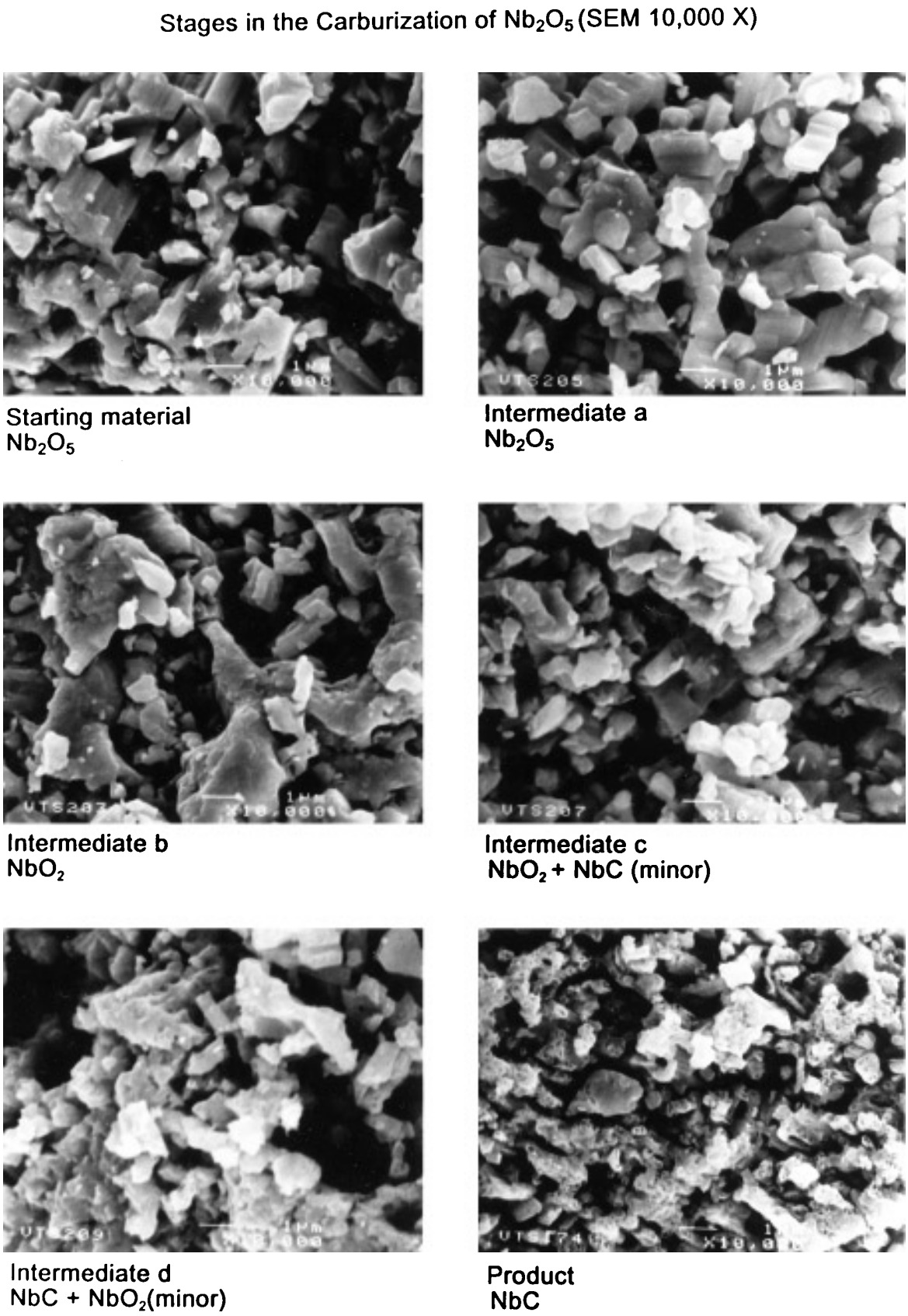

FIG. 8. Scanning electron microscopy pictures of commercial B-Nb_2O_5, NbC, and compounds obtained by interruption of the carburization reaction.

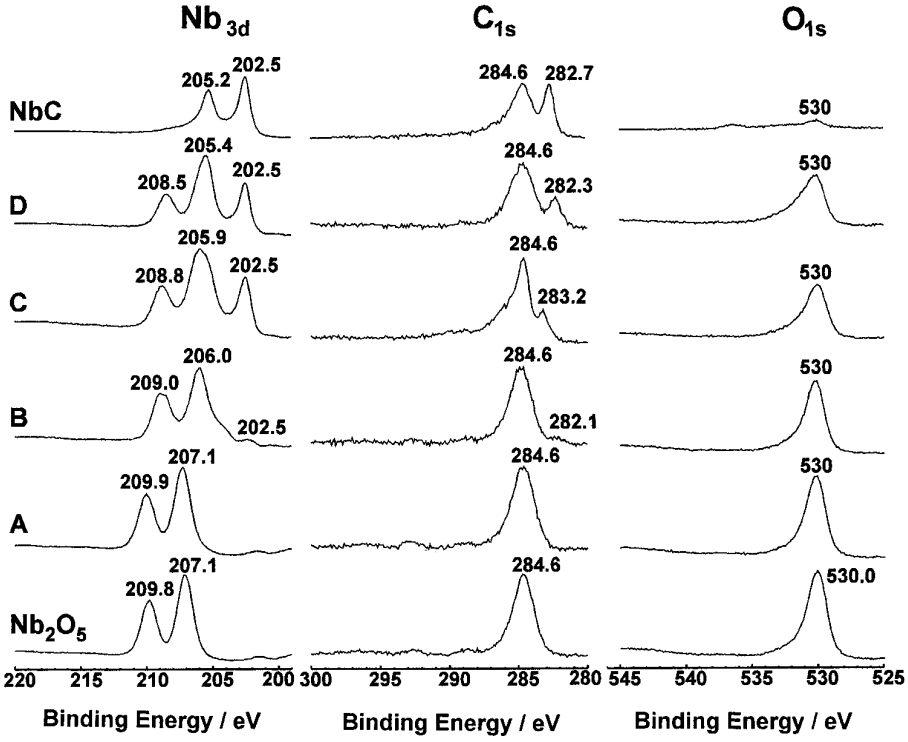

FIG. 9. X-ray photoelectron spectra of the Nb 3*d*, C 1*s*, and O 1*s* photopeaks for commercial B-Nb_2O_5, NbC, and compounds obtained by interruption of the carburization reaction.

Mo_2N, Table 2 shows that an increase in the molar space velocity by a factor of 4 (from 400 to 1600 h^{-1}) and a decrease in β (from 0.1667 to 0.0417 K s^{-1}) caused only small average increases in S_g of the synthesized samples of NbC. The insensitivity of S_g to variations in space velocity or heating rate observed in the synthesis of NbC is probably due to the high synthesis temperatures used of up to 1373 K. These conditions sinter the smaller crystallites as evidence by the fact that all of the obtained carbides had particle sizes (D_P) larger than the crystallite sizes (D_C), indicating particle agglomeration (Table 2).

Although the obtained carbides present S_g values nearly 1800% higher than that of the starting oxide, these values of S_g are low when compared to those of materials commonly used as catalysts. The increase in surface area when the solid-state transformation oxide → carbide takes place immediately raises the question of why or how S_g increases.

Volpe and Boudart (24) have concluded, for the case of Mo_2N, that the increase in surface area during MoO_3 nitridation is associated with the development of porosity during the reaction. Examination of SEM pictures (Fig. 8) shows that while the commercial Nb_2O_5 starting material is formed of large, dense crystallites (Fig. 8A), the NbC product particles (Fig. 8F) are permeated by holes or cracks with sizes bigger than 100 nm. The appearance of these macropores was not accompanied by changes in the solid's external form indicating, as observed in another NbC synthesis study (45), that the transformation $Nb_2O_5 \rightarrow NbC$ is a pseudomorphic process (24, 25).

Another negative feature of a high synthesis temperature is the deposition of "pyrolytic" carbon due to the thermal decomposition of methane (28). The term "pyrolytic" carbon is used here to describe surface carbon in amorphous, graphitic, coke, or other aggregate form as opposed to "carbidic" carbon which is the atomic carbon chemically bonded to niobium. In fact, Auger electron spectroscopy indicates that the surface carbon is in graphitic form (46).

Table 2 shows that all of the synthesized carbides have a carbon content of around 18 wt%. Since the theoretical content of carbon in NbC is 11.44 wt%, the amount obtained by TPO represents an excess of 57%. The excess carbon is probably deposited on the carbidic surface in a multi-layer form, corresponding to about 18 layers of graphite, and is probably responsible for the low CO uptakes presented in Table 2. Preliminary experiments indicate that the dense layer of pyrolytic carbon formed on the NbC surface does not contribute much to S_g (46). For example, it cannot be reduced by H_2 treatment even at 973 K, but it is mostly removed by O_2 treatment at 623 K without changes in S_g. Uptakes of CO on such samples (after reduction at 723 K) increase from 10 to 38 μmol g^{-1}

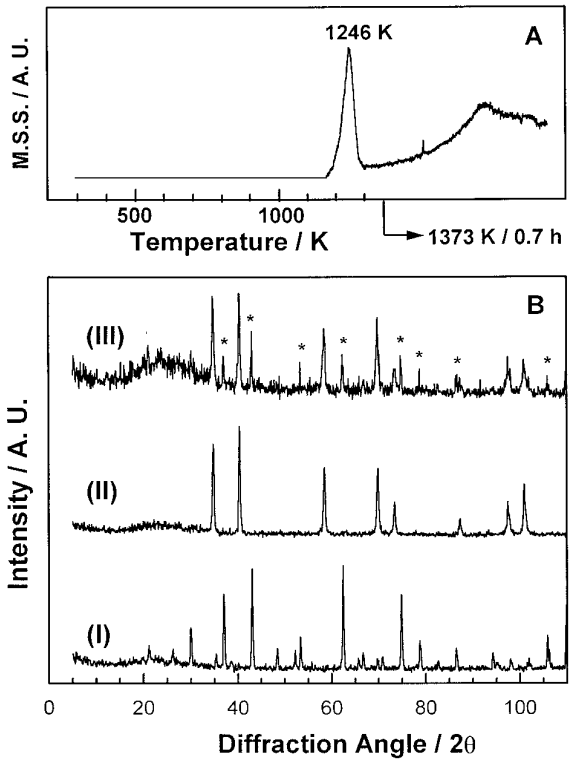

FIG. 10. (A) Carbon monoxide formation profile during TPR using NbO as precursor in the NbC synthesis (SV = 1600 h^{-1}; H.R. = 0.0417 K s^{-1}); (B) X-ray diffraction patterns of NbO (I), commercial NbC (II), and compound obtained by carburization of the NbO (III).

with S_g remaining constant at 18 m^2 g^{-1}. Since the pores formed during NbC synthesis are in the range of macropores, the pyrolytic carbon formed does not block them completely and does not affect S_g. One way to overcome the problem of excess carbon during NbC synthesis may be to carry out the synthesis with lower concentrations of methane (28), but in this case lower values of S_g would be expected (27).

Theory of the Synthesis Method

The application of temperature-programmed reaction theory to the water formation profiles presented in Fig. 1, 3, and 4 provides additional information on the solid-state transformation $Nb_2O_5 \rightarrow NbC$. For all of the synthesized carbides, the first water formation peak is located in the temperature-programmed region and has, depending on the conditions used, different values for the maxima (T_{max}). The Redhead equation (35) predicts that the transformation temperature, T_{max} (K), is related to the heating rate, β (K s^{-1}), by

$$2 \ln T_{max} - \ln \beta = E/RT_{max} + C, \qquad [1]$$

where E is the activation energy (J mol^{-1}), R is the universal gas constant (R = 8.314 J mol^{-1} K^{-1}), and C is a constant related to the characteristics of the solid, the reactive gas composition, and the kinetics of the transformation and contains units that make the left-hand side of the equation dimensionless.

The activation energy E can be determined simple by plotting values of (2 ln T_{max} − ln β) vs $1/T_{max}$ obtained for each space velocity (Fig. 12). Table 4 shows that the activation energy values of the reductive process associated with the first water formation peak are independent of the molar space velocity employed during the synthesis. The percentage error between the lower (98 kJ mol^{-1}) and the higher (105 kJ mol^{-1}) activation energy values is 7% and can be attributed to experimental error.

Since the diffraction pattern of the compound obtained when the carburization was interrupted at the end of the first water formation peak (point B in Fig. 6) reveals that the bulk crystallographic phase is composed mainly of NbO_2 (Fig. 7C), it can be concluded that the reductive process associated with the first water formation peak is simply a Nb_2O_5 reduction to NbO_2 with an activation energy in the range 98–105 kJ mol^{-1}.

Moreover, the fact that the presence of NbO_2 was observed either by XRD (Fig. 7C) or by XPS (Fig. 9C) for

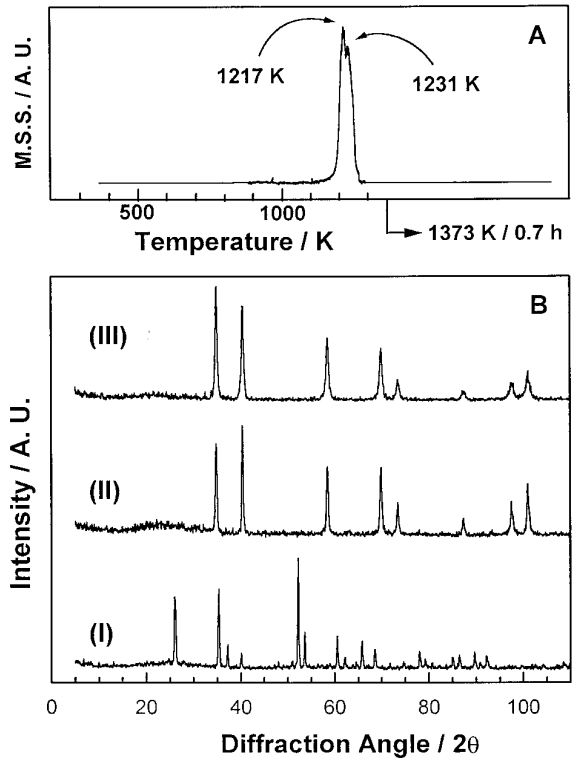

FIG. 11. (A) Carbon monoxide formation profile during TPR using NbO_2 as precursor in the NbC synthesis (SV = 1600 h^{-1}; H.R. = 0.0417 K s^{-1}); (B) X-ray diffraction patterns of NbO_2 (I), commercial NbC (II), and compound obtained by carburization of NbO_2 (III).

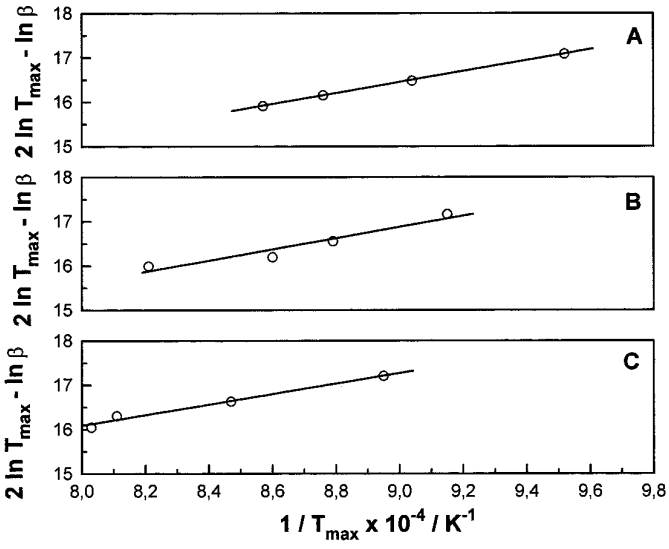

FIG. 12. (2 ln T_{max} − ln β) vs ($1/T_{max}$) plots for the experiments conducted using 400 h^{-1} (A), 800 h^{-1} (B), and 1600 h^{-1} (C).

the compound obtained by interruption of the reaction after the first water formation peak necessarily means that NbO_2 is an intermediate in the solid-state transformation $Nb_2O_5 \rightarrow NbC$.

The Redhead equation cannot be applied either to the second water formation peak or to the CO formation peak because for the majority of the experiments presented in Figs. 1, 3, and 4 these peaks are only partially located in the temperature-programmed region.

In TPR theory two mathematical models known as the Nucleation Model and Shrinking Core Model exist to describe the reduction of an oxide. The models assume spherical geometry and have been described in several reviews of the literature (35, 36). Briefly, the main differences between the two models are related to the kinetics of the reduction process. The Nucleation Model supposes that the reaction between the metal oxide and the hydrogen starts after an induction time, t_1, in which the first nucleus of the product forms. The oxygen atoms are removed either

TABLE 4

Activation Energy of the Reductive Process Associated with the First Water Formation Peak during the Commercial B-Nb_2O_5 Carburization

SV_{molar} (h^{-1})	E (kJ mol^{-1})
400	98
800	105
1600	102

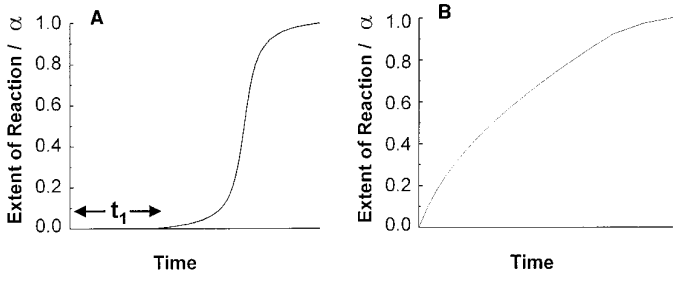

FIG. 13. Graphical comparison between the (A) Nucleation Model and (B) Shrinking Core Model.

through the diffusion of vacancies into the oxide lattice or through the diffusion of oxygen atoms out of the lattice. The reaction interface, which can be visualized as being the interface between the nucleus of the product and the unreacted solid, starts to grow more and more quickly after the induction period basically by two processes: (i) growth of the already formed nuclei and (ii) appearance of new nuclei. At a certain moment, the nuclei of product totally occupy the interface and consequently there is a decrease in the reaction rate. If the extent of reaction, α, is plotted against the reaction time, a curve with a sigmoidal shape is obtained.

On the other hand, the Shrinking Core Model suggests that the reaction's interface is maximum at the beginning of the reduction and decreases continuously as the reaction takes place. According to Hurst *et al.* (35), the reaction's interface is maximum in the beginning of the reduction due to a fast nucleation which takes place as soon as the hydrogen contacts the metal oxide and leads to the formation of a thin layer of product over the oxide. With the progress of the reaction, the thickness of the product increases continuously while the core of the metal oxide shrinks. If the extent of reaction α is plotted against the reaction time, the obtained curve has a parabolic-like shape.

A comparison of the curves obtained for the Nucleation and Shrinking Core models is presented in Fig. 13. The figure shows that the plots of α vs t for these two models are substantially different.

The type of reduction kinetics associated with the first water formation peak can be determined by simply plotting the extent of reaction α against the reaction time t for each of the experiments in Figs. 1, 3, and 4. Assuming that at the end of the first water formation peak the extent of reaction of the solid-state transformation $Nb_2O_5 \rightarrow NbO_2$ is equal to 1, the extent of reaction at each point can be obtained from the fractional area under the total peak and leads to the results presented in Fig. 14.

Due to the fact that the different experiments had different total times, the extent of reaction was plotted in Fig. 14 against a dimensionless time τ, defined as the ratio

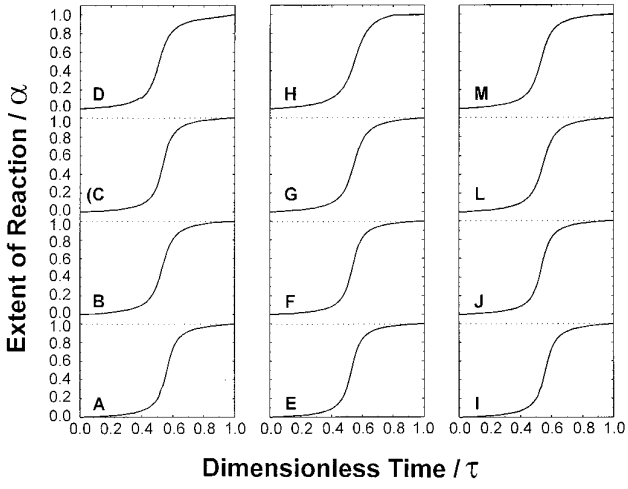

FIG. 14. Kinetics of reduction of the first water formation peak during the synthesis of (A) **400-10,** (B) **400-7.5,** (C) **400-5.0,** (D) **400-2.5,** (E) **800-10,** (F) **800-7.5,** (G) **800-5.0,** (H) **800-2.5,** (I) **1600-10,** (J) **1600-7.5,** (K) **1600-5.0,** and (L) **1600-2.5.**

between a specific reaction time and the total time necessary for a peak. From the comparison between the kinetic profiles presented in Figs. 14 and 13, it is clear that the reduction reaction $Nb_2O_5 \rightarrow NbO_2$ is described by the Nucleation Model.

Defining a dimensionless time $\tau_{0.5}$ as the time needed to achieve 50% of the reduction, Table 5 shows the values of $\tau_{0.5}$ obtained for each experiment in Fig. 14, and shows that, independently of the synthesis conditions, the values of $\tau_{0.5}$ are practically constant and equal to 0.5. This means that the reaction order is equal to 1 and the reductive process can be described by the equation (47, 48)

TABLE 5
Dimensionless Time $\tau_{0.5}$ for the Reduction Reaction Associated with the First Water Formation Peak

Experiment	$\tau_{0.5}$
400-2.5	0.499
400-5.0	0.501
400-7.5	0.502
400-10	0.500
800-2.5	0.500
800-5.0	0.501
800-7.5	0.504
800-10	0.503
1600-2.5	0.503
1600-5.0	0.505
1600-7.5	0.503
1600-10	0.506

$$\frac{d\alpha}{dT} = \frac{h^2 k_0}{\beta}(1-\alpha)^1 \exp\left(-\frac{E}{RT}\right), \qquad [2]$$

where α is the extent of reaction, T the temperature, k_0 the pre-exponential factor of the Arrhenius equation, E the activation energy, h the diameter of the particle, and R the gas constant. The term $(1 - \alpha)$ in the right-hand side of Eq. [2] has an exponent equal to 1 indicating that the reaction order relative to the solid is 1.

$Nb_2O_5 \rightarrow NbC$ Transformation Mechanism

Analysis of the diffraction patterns (Fig. 7) can be used to identify stable intermediates in the transformation of B-Nb_2O_5 to NbC. The diffraction pattern (Fig. 7A) of the product obtained by interruption of the reaction immediately after the formation of the first small water shoulder at 936 K (Fig. 6) is identical to the pattern of the B-Nb_2O_5 starting material. This small shoulder situated between 850 and 936 K in the water formation profile (Fig. 6) could be associated either with a surface reduction of the B-Nb_2O_5 precursor forming small reduced particles not detectable by XRD, or to a desorption of hydroxyl groups strongly bonded to the oxide surface. Since the Nb 3*d* photopeak of product A in Fig. 9A does not show any differences when compared with the B-Nb_2O_5 starting material, the elimination of hydroxyl groups seems plausible.

As discussed before, the first water formation peak corresponds to the reduction reaction B-$Nb_2O_5 \rightarrow NbO_2$ and follows the nucleation (35, 36) kinetic model. However, when the Nb 3*d* spectrum of the product obtained by interruption of the carburization reaction at 1163 K is analyzed (Fig. 9B), it can be seen that besides the photopeaks associated with NbO_2 of binding energies of 206.0 eV ($Nb_{3d5/2}$) and 209.0 eV ($Nb_{3d3/2}$), there is a small photopeak related to NbC with energy 202.5 eV (41). This means that at the initial stages of the second reductive process (second water formation peak) which begins simultaneously with the carburization process (carbon monoxide formation), the product present in the reactor is NbO_2 with a small amount of NbC. Because transition metal carbides have metallic character (1, 14), the NbC traces mixed with NbO_2 could promote hydrogen activation by spillover (49) which would lead to a higher degree of NbO_2 reduction than if NbC were absent. However, hydrogen activation by this NbC probably does not occur, since it was observed that the intermediate B had a null CO uptake (Table 3).

Because CO chemisorption in NbC is linear (50), even a small amount of NbC as shown by XPS should result in some CO uptake. However, since methane decomposition is thermodynamically favored at the temperature where product B was obtained, i.e., 1163 K (26), the observation of a null CO uptake indicates that the carbidic sites are

already covered by pyrolytic carbon. So, the second water formation peak during the B-Nb_2O_5 carburization has to be explained in another way.

The interruption of the carburization reaction at 1267 K (point C in Fig. 6) did not result by XRD analysis in any niobium oxide with metal oxidation number lower than +4. Instead, Fig. 7C shows that there was an intensity decrease in the reflections of NbO_2 and the appearance of weak reflections due to NbC. The interruption of the reaction at the end of the second water formation peak at 1337 K (point D in Fig. 6) caused an almost complete disappearance of the NbO_2 reflections and an intensity increase of those characteristic of NbC. As shown in Table 3, the appearance of NbC occurs with increases in the S_g and CO uptake values.

The observation of NbC (point C in Fig. 6) and at the end (point D in Fig. 6) of the second water formation profile is consistent with the results in Figs. 1, 3, and 4 that showed simultaneous carbon monoxide formation. The coexistence of a mixture NbO_2/NbC during the second water formation peak is confirmed when the Nb 3*d* and C 1*s* XPS spectra are analyzed: intermediates C and D have the NbC characteristic doublet and C singlet in the binding energies of 202.5 and 283.2 eV, respectively.

The second water formation peak is clearly associated with a reduction of the NbO_2. However, the lack of any reflections due to a lower oxide (Patterns C and D, Fig. 7) indicates that if such an oxide were formed its thickness would be less than 4 nm and therefore not detectable by XRD or, if formed, would be quickly carburized to NbC.

The experiment where NbO was used as starting material in the NbC synthesis (Fig. 10) reveals that the oxide was not completely carburized to NbC using the same synthesis conditions as those employed when Nb_2O_5 or NbO_2 were used as precursors. However, the fact that only a small part of the NbO undergoes transformation forming NbC does not eliminate it as a reaction intermediate because if only a small amount of NbO_2 was transformed to NbO, this small NbO amount could be transformed to NbC.

Nevertheless, the NbO formation hypothesis is not supported by the XPS spectra of intermediates C and D in Fig. 9C and 9D. According to Fontaine *et al.* (40), the NbO XPS signal for the $Nb_{3d5/2}$ photopeak corresponds to a binding energy of 204.5 eV. Since such a value was not observed in the XPS spectra of the intermediates C and D, the NbO formation hypothesis is discarded.

As shown in Fig. 9, the XPS spectra of intermediates C and D present maxima for the $Nb_{3d5/2}$ photopeak in 205.9 and 205.4 eV, respectively. These values of binding energies are intermediate to those presented by NbO_2 (206.0 eV) and NbO (204.5 eV) and could suggest the presence of an niobium oxide with the metal having oxidation number between +4 and +2, i.e., an oxide of the type of NbO_x with $2 < x < 1$. Niobium oxides of such stoichiometry do not exist in the inorganic chemistry literature (51).

Thus, the only possible explanation for the occurrence of the second water formation peak is that the NbO_2 is transformed to NbC, through the formation of a reactive intermediate, which is suggested to be an oxycarbide NbO_xO_y. Schematically,

$$\text{B-Nb}_2\text{O}_5 \xrightarrow[\text{fast}]{} \text{NbO}_2 \xrightarrow[\text{slow}]{} [\text{NbO}_x\text{C}_y] \xrightarrow[\text{fast}]{} \text{NbC}.$$

The first step involving the formation of the stable NbO_2 intermediate is supported by the experiment in which NbO_2 itself was carburized (Fig. 12). The proposed mechanism is also consistent with the observation of only NbO_2 and NbC in the XRD diffraction patterns of intermediates C and D in Fig. 9.

Although XRD provides no direct evidence of the NbO_xC_y intermediate, the XPS spectra presented in Fig. 9 provide an indication for its presence. The figure shows that while the Nb_2O_5 $Nb_{3d5/2}$ photopeak has a binding energy of 207.1 eV, the NbC $Nb_{3d5/2}$ photopeak has a binding energy of 202.5 eV. This displacement in the position of the $Nb_{3d5/2}$ photopeak to lower binding energy values also occurs in the series of intermediates B (206.0 eV), C (205.9 eV), and D (205.4 eV). As just discussed, these binding energies do not correspond to a suboxide, and are assigned to the oxycarbide intermediate.

Ramqvist *et al.* (41) have observed that the maximum associated to the $Nb_{3d5/2}$ photopeak was displaced by 0.24 eV to lower binding energies when the carbon content in NbC was varied from $NbC_{0.744}$ to $NbC_{0.940}$. Thus, in the region of reaction which includes intermediates C and D (1267–1337 K) there is a progressive carbon enrichment in the oxycarbide NbO_xC_y resulting in the 0.5 eV displacement observed for the $Nb_{3d5/2}$ photopeak.

Assuming that the second water formation peak is associated with the transformation of a fraction of the NbO_2 to an oxycarbide NbO_xC_y, it rests to determine if the oxycarbide is transformed to NbC by reduction (H_2O formation) or by carburization (CO formation). If the solid-state transformation $NbO_xC_y \rightarrow$ NbC occurred by means of a reductive process, then a third water formation peak should be seen. Since the water formation profile presents only two peaks, the oxycarbide transformation to NbC is likely to occur through a carburizing process. Moreover, this step must be fast when compared to the formation step since the NbO_xC_y is not observed in bulk quantities by XRD.

CONCLUSIONS

Using the temperature-programmed reaction between B-Nb_2O_5 and 20% (v/v) CH_4/H_2 mixture it is possible to

synthesize niobium carbide with specific surface areas (S_g) of 20 m^2 g^{-1}. However, increasing molar space velocity or decreasing heating rate does not lead to substantial increases in S_g of the product. The insensitivity of S_g to the synthesis variables is due to the high temperature of synthesis that lead to the sintering of some of the crystals. The high temperatures also lead to the thermal decomposition of methane and the deposition of "pyrolytic" carbon. The pyrolytic carbon consists of more or less organized graphitic domains that inhibit the chemisorption of CO on the synthesized carbides.

As observed by mass spectroscopy and XRD, the solid-state transformation B-$Nb_2O_5 \rightarrow$ NbC occurs in two steps: (i) reduction to NbO_2 with an activation energy in the range 98–105 kJ mol^{-1}, and (ii) simultaneous reduction and carburization to NbC. The first reductive process follows a nucleation kinetic model. XPS analysis further reveals the presence of an oxycarbide phase which is an intermediate in the transformation of NbO_2 to NbC. The overall transformation is

$$\text{B-Nb}_2\text{O}_5 \rightarrow \text{NbO}_2 \rightarrow [\text{NbO}_x\text{C}_y] \rightarrow \text{NbC}.$$

SEM photographs indicate that the transformation is a pseudomorphic process with preservation of the external form of the starting material.

ACKNOWLEDGMENTS

This paper was written with support from the U.S. Department of Energy Grant DE-PS22-95PC95207. One of us (VTS) is grateful to CNP_q (Conselho Nacional de Desenvolvimento Cientifico e Tecnológico, Brazil) for the scholarship received during the development of this work.

REFERENCES

1. L. E. Toth, "Transition Metal Carbides and Nitrides." Academic Press, New York, 1971.
2. M. Boudart, S. T. Oyama, and L. Leclercq, *in* "Proceedings, 7th International Congress on Catalysis, Tokyo 1980" (T. Seiyama and K. Tanabe, Eds.), Vol. 1, p. 578. Elsevier, Amsterdam, 1981.
3. I. Kojima, E. Miyazaki, Y. Inoue, and I. Yasumori, *J. Catal.* **59,** 473 (1979).
4. I. Kojima, E. Miyazaki, Y. Inoue, and I. Yasumori, *J. Catal.* **73,** 128 (1982).
5. B. Vidick, J. Lemaître, and L. Leclercq, *J. Catal.* **99,** 439 (1986).
6. M. Saito and R. B. Anderson, *J. Catal.* **63,** 438 (1980).
7. M. Saito and R. B. Anderson, *J. Catal.* **67,** 296 (1981).
8. F. H. Ribeiro, R. A. Dalla Betta, M. Boudart, J. E. Baumgartner, and E. Iglesia, *J. Catal.* **130,** 86 (1991).
9. F. H. Ribeiro, R. A. Dalla Betta, M. Boudart, and E. Iglesia, *J. Catal.* **130,** 543 (1991).
10. F. H. Ribeiro, E. Iglesia, J. E. Baumgartner, and M. Boudart, *J. Catal.* **131,** 523 (1991).
11. M. J. Ledoux, C. Pham-Huu, H. Dunlop, and J. Guille, *in* "Proceedings, 10th International Congress on Catalysis" (L. Guczi, F. Solymosi, and P. Tétényi, Eds.). Akadémiai Kiadó, Budapest, 1993.
12. J. S. Lee and M. Boudart, *Appl. Catal.* **19,** 207 (1985).
13. D. J. Sajkowsky and S. T. Oyama, Preprints, Division of Petroleum Chemistry, Symposium on "The Chemistry of W/Mo Catalysts", 199th ACS National Meeting, Boston, MA, April 22–27, 233 (1980).
14. J. C. Schlatter, S. T. Oyama, J. E. Metcalfe III, and J. M. Lambert Jr., *Ind. Eng. Chem. Res.* **27,** 1648 (1988).
15. L. T. Thompson, C. W. Cooling, D. Choi, B. G. Demczyk, and J. G. Choi, *in* "Proceedings, 10th International Congress on Catalysis" (L. Guczi, F. Solymosi, and P. Tétényi, Eds.). Akadémiai Kiadó, Budapest, 1993
16. E. J. Markel and J. W. van Zee, *J. Catal.* **126,** 643 (1990).
17. K. S. Lee, H. Abe, J. A. Reimer, and A. T. Bell, *J. Catal.* **139,** 34 (1993).
18. H. Abe and A. T. Bell, *Catal. Lett.* **18,** 1 (1993).
19. M. Nagai, T. Miyao, and T. Tuboi, *Catal. Lett.* **18,** 9 (1993).
20. H. Abe, T. K. Cheung, and A. T. Bell, Preprints, Division of Petroleum Chemistry, ACS, Symposium on "Mechanism of HDS/HDN reactions", Chicago, Il, August 22–27, **38-3,** 668 (1993).
21. M. Nagai, T. Miyao, and A. Miyata, Preprints, Division of Petroleum Chemistry, ACS, Symposium on "Mechanism of HDS/HDN reactions," Chicago, Il, August 22–27, **38-3,** 669 (1993).
22. S. T. Oyama, Ph.D. Dissertation, Stanford University, Stanford, CA, 1981.
23. L. Volpe, S. T. Oyama, and M. Boudart, *in* "Preparation of Catalysts III" (G. Poncelet, P. Grange, and P. A. Jacobs, Eds.), p. 147. Elsevier, Amsterdam, 1983.
24. L. Volpe and M. Boudart, *J. Solid State Chem.* **59,** 332 (1985).
25. L. Volpe and M. Boudart, *J. Solid State Chem.* **59,** 348 (1985).
26. J. S. Lee, S. T. Oyama, and M. Boudart, *J. Catal.* **106,** 125 (1987).
27. S. T. Oyama, J. C. Schlatter, J. E. Metcalfe III, and J. M. Lambert Jr., *Ind. Eng. Chem. Res.* **27,** 1639 (1988).
28. J. S. Lee, S. Locatelli, S. T. Oyama, and M. Boudart, *J. Catal.* **125,** 157 (1990).
29. G. S. Ranhotra, G. W. Haddix, A. T. Bell, and J. A. Reimer, *J. Catal.* **108,** 24 (1987).
30. J. S. Lee, M. H. Yeom, K. Y. Park, I. S. Nam, J. S. Chung, Y. G. Kim, and S. H. Moom, *J. Catal.* **128,** 126 (1991).
31. E. K. Storms, "The Refractory Carbides." Academic Press, New York and London, 1967.
32. J. F. Smith, O. N. Carlson, and R. R. De Avillez, *J. Nucl. Mater.* **148,** 11 (1987).
33. P.Ettmayer and W. Lengauer, *in* "Encyclopedia of Inorganic Chemistry" (R. B. King, Ed.), Vol. 2, p. 519. Wiley, Chichester, 1994.
34. S. Brunauer, P. H. Emmet, and E. J. Teller, *J. Am. Chem. Soc.* **60,** 309 (1938).
35. N. W. Hurst, S. J. Gentry, A. Jones, and B. D. McNicol, *Catal. Rev.-Sci. Eng.* **24,** 233 (1982).
36. J. L. Falconer and K. A. Schwartz, *Catal. Rev.-Sci. Eng.* **25,** 141 (1983).
37. Powder Diffraction Data File 38-1364, Inorganic Phases, JCPDS International Center for Diffraction Data, Swathmore, PA, 1981.
38. G. E. McGuire, G. K. Schweitzer, and T. A. Carlson, *Inorg. Chem.* **12,** 2451 (1973).
39. V. I. Nefedov, D. Gati, B. F. Dzhurinskii, N. P. Sergushin, and Y. V. Salyn, *Zh. Neorg. Khim.* **20,** 2307 (1975).
40. R. Fontaine, R. Caillat, L. Feve, and M. Guittet, *J. Electr. Spectros.* **10,** 349 (1977).
41. L. Ramqvist, K. Hamrim, G. Johansson, U. Gelius, C. Nordling, *J. Phys. Chem. Solids* **31,** 2669 (1970).
42. R. S. Wise and E. J. Markel, *J. Catal.* **145,** 335 (1994).
43. J. G. Choi, R. L. Curl, and L. T. Thompson, *J. Catal.* **146,** 218 (1994).
44. R. Kapoor and S. T. Oyama, *J. Solid State Chem.* **99,** 303 (1992).
45. V. L. S. Teixeira da Silva, E. I. Ko, M. Schmal, and S. T. Oyama, *Chem. Mater.* **7,** 179 (1995).
46. V. L. S. Teixeira da Silva, D. Sc. Dissertation Thesis, Programa de Engenharia Química, COPPE, Universidade Federal do Rio de Janeiro, Rio de Janeiro, RJ, 1994.

47. J. L. Lemaitre, *in* ''Characterizations of Heterogeneous Catalysts'' (F. Delanay, Ed.), p. 21. Dekker, New York and Basel, 1984.
48. S. Bathia, J. Beltramini, and D. D. Do, *Catal. Today* 7**(3),** 309 (1990).
49. M. Boudart, M. A. Vannice, and J. E. Benson, *Z. Phys. Chem. W. F.* **64,** 171 (1969).
50. K. Edamoto, E. Shiobara, T. Anazawa, M. Hatta, E. Miyazaki, H. Kato, and S. Otani, *J. Chem. Phys.* 96**(1),** 842 (1992).
51. C. N. R. Rao and G. V. Subba Rao, ''Transition Metal Oxides-Crystal Chemistry, Phase Transformation and Related Aspects.'' National Standard Reference Data System, U.S. Department of Commerce, Washington, DC, 1974; H. Lehl, ''Gmelins Handbuch der Anorganischen Chemie, Niob, System-Nummer 49.'' Verlag Chemie, Weinheim, 1970; F. A. Cotton, and G. Wilkinson, ''Advanced Inorganic Chemistry,'' 5th ed. Wiley, New York, 1988.